Available online at www.sciencedirect.com
SCIENCE DIRECT®
International Journal of Heat and Fluid Flow 25 (2004) 471–480
International Journal of HEAT AND FLUID FLOW
www.elsevier.com/locate/ijhff

The modifications of near-wall turbulence structure and heat transfer by immiscible droplets in turbulent liquid–liquid two-phase flow

Takuji Yuge, Yoshimichi Hagiwara *

Department of Mechanical and System Engineering, Kyoto Institute of Technology, Goshokaido-cho, Matsugasaki, Sakyo-ku, Kyoto 606-8585, Japan

Abstract

Direct numerical simulation based on finite difference schemes has been carried out for non-isothermal turbulent upward channel flow with four immiscible droplets whose density is higher than that of continuous-phase liquid. The interface was tracked by the modified volume-of-fluid method. The computational results show that both the outward flow in the wake and the wallward flow around the cap of droplets enhance heat transfer. These flows are attenuated by the adjacent droplet in the axial direction. The droplets deform large-scale streamwise vortices and attenuate small-scale streamwise vortices.

Keywords: DNS; Immiscible droplets; Turbulence modification; Coherent structure; Heat transfer enhancement

1. Introduction

Flow characteristics and heat transfer of turbulent liquid flow with immiscible droplets have been the focus of recent research. It is crucial to elucidate this phenomenon for developing a liquid–liquid direct-contact heat exchanger. This new heat exchanger provides one of the most effective equipments for the recovery of exhaust heat in warm water from buildings and factories with temperature close to the ambient in order to use energy efficiently and thus help protect the environment (Kadoguchi, 2002). Lee (1987) measured the droplet size distribution and the overall heat transfer coefficient in the direct-contact process. Kaviany (1994) investigated the interaction between a droplet and its surrounding flow. Inaba et al. (1998) obtained empirical equations for the size distribution of droplets injected into water flow and inter-phase heat transfer. These results all provide useful data for designing the heat exchanger.

However, the effect of a wall on the flow characteristics and heat transfer of the dispersed liquid–liquid two-phase flow was not considered in these studies. This is because the droplets were located far from the wall in these studies. To consider the effect is crucial for developing a small-scale heat exchanger. The present authors concluded from their simulation that the outward component of the wake flow of a counter-moving droplet induces the liftup of the fluid with high temperature adjacent to the heating wall in turbulent downward flow (Hagiwara et al., 2003) or upward flow (Hagiwara et al., 2001). We also showed that the wallward component of the impinging flow on the rising droplet cap brings low-temperature fluid into the near-wall region in each case. These studies dealt with only one droplet.

In the present numerical study, we carry out a direct numerical simulation of turbulent heat transfer in upward channel flow with four droplets of high density. We focus on the interaction between near-wall turbulence structures and the droplets and discuss heat transfer associated with this interaction.

2. Computational domain and grid arrangement

Fig. 1 indicates the computational domain. The domain was a rectangular box in a turbulent flow between two vertical walls at the distance of $2h$. The origin of the coordinate was set at a bottom corner of the domain.

* Corresponding author. Tel.: +81-75-724-7324; fax: +81-75-724-7300.
E-mail address: yoshi@ipc.kit.ac.jp (Y. Hagiwara).

0142-727X/$ - see front matter © 2004 Elsevier Inc. All rights reserved.
doi:10.1016/j.ijheatfluidflow.2004.02.014

Nomenclature

C	center for spherical interface
c_p	specific heat at constant pressure
F	fraction of continuous-phase fluid
$\overline{F}$	average value of F over the specific domain
f_i	interfacial tension force per unit volume
g	gravitational acceleration
h	half of the wall distance
L_x, L_z	size of computational domain
M	total number of points of intersection between spherical surface and sides of cell
N	points of intersection between spherical surface and side of cell
$\boldsymbol{n}$	unit vector normal to the interface
Pr	Prandtl number
p	pressure
q	heat flux
q_w	wall heat flux
R	radius of a spherical interface
Re	Reynolds number
S	interface area
t	time
$\bar{u}_1$	streamwise mean velocity
$(u_1, u_2, u_3) = (u, v, w)$	velocities in the streamwise, wall-normal and transverse directions
u', v', w'	fluctuating velocity components
u'_{rms}, v'_{rms}, w'_{rms}	root-mean-square of fluctuating velocity components
u_τ	friction velocity
$-\overline{u'v'}$	Reynolds shear stress
$-u'v'$	Reynolds-shear stress product
$\overline{v'\theta'}$	turbulent heat flux
$-v'\theta'$	product of wall-normal velocity fluctuation and temperature fluctuation
$(x_1, x_2, x_3) = (x, y, z)$	coordinates in the streamwise, wall-normal and transverse directions

Greeks

Δx	grid spacing in the x-direction
$\Delta\tilde{x}$	dimension of fine cubic cell
$\Delta y(y)$	grid spacing in the y-direction
Δz	grid spacing in the z-direction
δ	Kronecker delta
Θ	transformed temperature
θ'	temperature fluctuation
θ_τ	friction temperature
μ	viscosity
ν	kinematic viscosity
ρ	density
σ	interfacial tension coefficient
τ	viscous stress
ω	vorticity

Superscripts and subscripts

+	value made dimensionless with the wall parameters u_τ and ν
*	average value over the specific domain described in Section 5
c	continuous-phase
d	droplet
m	point for the intersection

The x, y and z axes were positioned in the streamwise (i.e. opposite to the direction of gravity), wall-normal and transverse directions, respectively. The domain size was $8h \times 2h \times 4h$.

The domain was divided into $128 \times 100 \times 128$ rectangular cells of volume of $\Delta V = \Delta x \times \Delta y(y) \times \Delta z$. Δx and Δz $(= \Delta x/2)$ were unchanged, while $\Delta y(y)$ was taken as $\Delta y(y) = \Delta z$ for $0.25 \leqslant y/h \leqslant 1.75$, $\Delta y(y) = \Delta z/2$ for $0.125 \leqslant y/h \leqslant 0.25$ and $1.75 \leqslant y/h \leqslant 1.875$, $\Delta y(y) = \Delta z/4$ for $0.016 \leqslant y/h \leqslant 0.125$ and $1.875 \leqslant y/h \leqslant 1.984$, and $\Delta y(y) = \Delta z/8$ for $0 \leqslant y/h \leqslant 0.016$ and $1.984 \leqslant y/h \leqslant 2$.

The velocity components were defined at the center of the cell surface (hereafter called grid points), while the pressure and external forces were defined at the center of the cell (hereafter called grid points for pressure and forces). The temperature was defined at the same location of the wall-normal velocity.

In order to improve the accuracy of the interface position, the original cells were further divided into fine

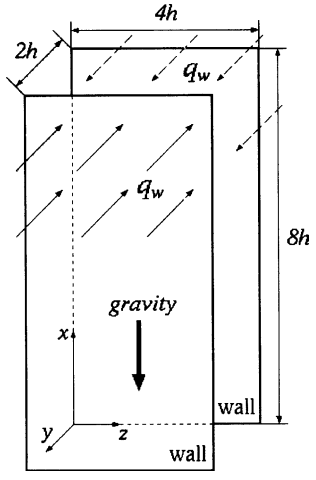

Fig. 1. Computational domain.

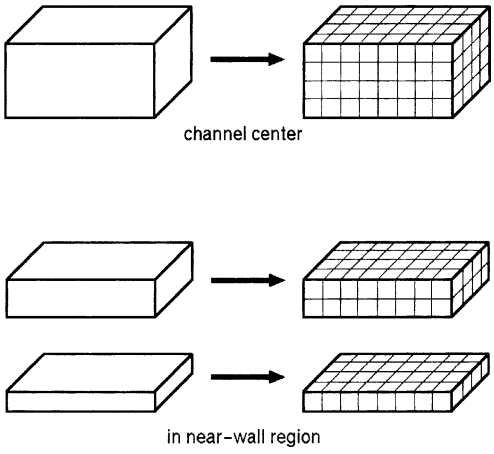

Fig. 2. Local grid refinement.

cubic cells in a region containing the droplets. The sides of the cubic cells were $\Delta\tilde{x} = \Delta x/8$ as shown in Fig. 2 based on our previous study (Tanaka et al., 1997). The fraction of the continuous-phase liquid, F, occupying a cell was defined at the center of the cubic cell.

The Reynolds number, Re_τ, based on the friction velocity, u_τ, was 180. The Prandtl number for continuous-phase fluid, Pr_c, was set equal to 2.0. In Table 1, the domain size, the grid spacing, the Reynolds numbers and the Prandtl number are compared with those adopted in direct numerical simulations for channel flows without droplets carried out by Kim and Moin (1989) and Kuroda and Kasagi (1992) with a spectral method and Kawamura et al. (1998) with a finite difference scheme.

3. Computational schemes

The equation of continuity and the following equations were discretized with the grid system mentioned above:

$$\rho^* \frac{\partial u_i}{\partial t} = -\rho^* u_k \frac{\partial u_i}{\partial x_k} - \frac{\partial p}{\partial x_i} + \frac{\partial \tau_{ij}}{\partial x_i} + g(\rho^* - \rho_c)\delta_{i1} + f_i,$$

$$\tau_{ij} = \mu^* \frac{\partial u_j}{\partial x_i}, \tag{1}$$

$$\rho^* \frac{\partial c_p^* \Theta}{\partial t} = -\rho^* u_k \frac{\partial c_p^* \Theta}{\partial x_k} - \frac{\partial q_i}{\partial x_i} + \frac{2q_w \bar{u}_1}{\int_0^{2h} \bar{u}_1 \, dx_2},$$

$$q_i = -\frac{c_p^* \mu^*}{Pr^*} \frac{\partial \Theta}{\partial x_i}, \tag{2}$$

where $(x_1, x_2, x_3) = (x, y, z)$, $(u_1, u_2, u_3) = (u, v, w)$, p, τ_{ij} are the coordinate, the velocity, the pressure and the viscous stress, respectively, ρ_c is the density of the continuous-phase liquid, g is the gravitational acceleration, and δ is the Kronecker delta. The fourth term in the right side of Eq. (1) is associated with the effect of the gravity on the droplets. The interfacial tension force f_i was evaluated by the procedure described in Section 6. q_i and q_w are the conductive heat flux and the wall heat flux, respectively. Θ is the transformed temperature (Kawamura et al., 1998). $\bar{u}_1$ is the streamwise mean velocity, ρ^*, μ^*, c_p^* and Pr^* are the average values of the density, the viscosity, the specific heat at constant pressure and the Prandtl number over the specific domain described in Section 5, respectively. The last term in the right side of Eq. (2) is associated with the linear increase of the mixed mean temperature in the streamwise direction (Kawamura et al., 1998). These equations were solved over the whole computational domain including the inside of the droplets.

We adopted the same schemes as those used in our previous study (Iwasaki et al., 2001): The second-order central difference scheme based on the interpolation method was applied in the finite differencing of the convection terms of Eq. (1). The second-order central difference scheme without the interpolation method was applied for the finite differencing of the viscous terms of the momentum equations and the energy equation. Poisson's equation for the pressure field was solved directly by using Fast Fourier Transforms and Gaussian elimination methods. The third-order Runge–Kutta method was used for the time-integration of the convective, viscous, and forcing terms in NS equations and the diffusion terms of energy equations.

In the wall-normal direction, the non-slip boundary condition was imposed for velocity components. Similarly, the Neumann boundary condition was given for the pressure. The constant wall temperature and the constant wall heat flux were assumed. The periodical boundary conditions were given for all the variables in the streamwise and transverse directions.

Table 1
Comparison of domain size and grid spacing

	$L_x \times L_z$	$\Delta x^+ \times \Delta y^+(y) \times \Delta z^+$	Re_τ	Pr
Kim and Moin	$4\pi h \times 2\pi h$	$18 \times 0.05 - 4.4 \times 8.8$	180	2, 0.71, 0.1
Kuroda and Kasagi	$12.8h \times 6.4h$	$18 \times \mathrm{NA} \times 9$	180	–
Kawamura et al.	$6.4h \times 3.2h$	$9 \times 0.40 - 11.5 \times 4.5$	180	1.5, 1.0, 0.71, ...
Present	$8h \times 4h$	$11.3 \times 0.70 - 5.6 \times 5.6$	180	2

4. Modified VOF algorithm

The position of the interface was determined by F; $F = 1$ represents a cell filled with the continuous-phase fluid, while $F = 0$ indicates that the cell is filled with the fluid of the droplet. The cells of $0 < F < 1$ include the interface. The time evolution of F was estimated with the modified volume of fluid (VOF) algorithm (Hirt and Nichols, 1981). We classified the intersection of the interface to the surfaces of the cubic cell (figure omitted). In the case when the interface intersected two parallel surfaces of the cell, the value of F was determined by the Donor–Accepter method. We took account of the slope of the interface in this method. In the other cases, we solved the following convection equation:

$$\frac{\partial F}{\partial t} = -u_i \frac{\partial F}{\partial x_i}. \tag{3}$$

The second-order central difference schemes were used for the spatial-differencing of Eq. (3). The values of the velocity components at the grids of the cubic cell for Eq. (3) were estimated firstly by linear interpolation of the velocity components of the original cells, and then the estimated velocity was corrected so that the equation of continuity was satisfied for each cubic cell at any time step.

5. Evaluation of physical properties near the interface

The local value of the physical property, φ^* ($= \rho^*$, μ^*, c_p^* or Pr^*), was evaluated as

$$\varphi^*(x_i) = \overline{F}(x_i)\varphi_c + (1 - \overline{F}(x_i))\varphi_d, \tag{4}$$

where φ_c and φ_d are the property for the continuous-phase liquid and that of the droplet respectively, and $\overline{F}$ is the average of F over the specific domain where the velocity, temperature, velocity gradient or temperature gradient is defined and is multiplied with φ^*. For example, in the case of ρ^* and μ^* for the three components of velocity gradient $(\partial u_i/\partial x_i)$, $\overline{F}$ is the average of F over the original cell whose center is located at **x1** as shown in Fig. 3. In the case of μ^* for the two components of velocity gradient ($\partial u_1/\partial x_2$ and $\partial u_2/\partial x_1$), $\overline{F}$ is the average of F over the domain whose dimension is the same as the original cell and whose center is located at **x2** (the box drawn by the broken lines) in Fig. 3.

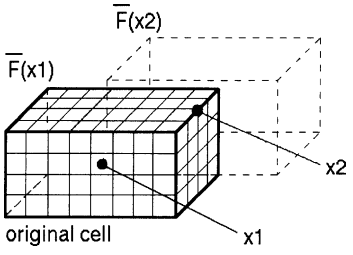

Fig. 3. Boxes and points for evaluation of viscosity.

6. Interfacial tension

The interfacial tension force in Eq. (1) was calculated by the following procedure, which is the same as that described in our previous study (Iwasaki et al., 2001). Let N_m $(m = 1, 2, \ldots, M)$ being the points of intersections between the spherical surface, which approximates to the interface (see Fig. 4). Here, the unit vector normal to the interface, $\boldsymbol{n}$, was estimated as

$$\boldsymbol{n} = \sum_{m=1}^{M} \boldsymbol{n}_m \Bigg/ \left| \sum_{m=1}^{M} \boldsymbol{n}_m \right|$$

where $\boldsymbol{n}_m = \vec{CN}_m$ $(m = 1, 2, \ldots, M)$ and C denotes the center of the sphere. The area of the spherical surface, S, was approximated by the sum of those of triangles which consist of the points N_m $(m = 1, 2, \ldots, M)$, and the point of intersection between the spherical surface and the normal vector. Using S and the radius R of the sphere obtained above, the interfacial tension force was calculated as

$$f_i \cdot \Delta V = \sigma(2/R)S(-n_i), \tag{5}$$

where ΔV is the cell volume, σ is the coefficient of the interfacial tension and n_i is the ith axial component of the unit vector.

7. Computational condition for droplets

We introduced four identical droplets with diameters of $6\Delta x$ $(= 48\Delta\tilde{x} = 67.5\nu/u_\tau)$ into near-wall region. At the initial state, the centers of all the droplets were allocated at the vertices of a square whose one-side length was 154 wall units and distance from one wall was 73 wall units. The initial fields of velocity and temperature inside the

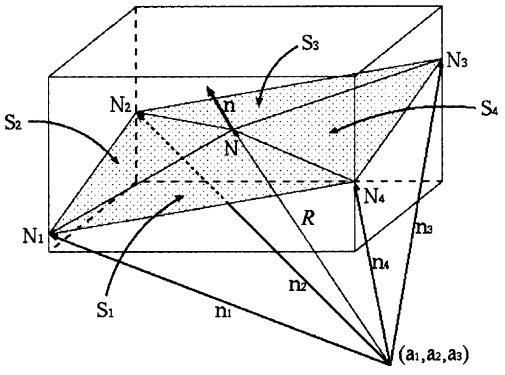

Fig. 4. Estimation of interfacial area and curvature.

Table 2
Physical properties

	Present computation	Hydrofluoroether (3M Novec, HFE7200)
Interfacial tension, σ^+	2160	9100
Density ratio, ρ_d/ρ_c	1.43	1.43
Viscosity ratio, μ_d/μ_c	30	0.65
Specific-heat ratio, C_{p_d}/C_{p_c}	0.29	0.29
Prandtl-no. ratio, Pr_d/Pr_c	1	1.66

droplets were the same as those at the same regions of single-phase flow.

We considered water for the continuous phase fluid and hydrofluoroether for the dispersed phase fluid. The computational condition for the droplet properties are compared with those of hydrofluoroether droplet in Table 2. Note that the interfacial tension was lower than the actual value in order to reduce the effect of high value of the external force on the stability of computation for Eq. (1). In addition, the viscosity was higher than the actual value in order to reduce the enhancement of deformation of the droplets due to the low value of the interfacial tension.

8. Results and discussion

8.1. Turbulence statistics

The turbulence statistics of single-phase flow were calculated for a period of $1800v/u_\tau^2$ before the initial field of velocity and temperature was obtained. It was confirmed that the mean velocity profile obtained in the present study is in agreement with that obtained by Kuroda and Kasagi (1992) with the spectral method (figure omitted). Fig. 5(a) and (b) indicate the profiles of turbulence intensities in the streamwise, wall-normal and transverse directions, and the profiles of the viscous shear stress, $\mu(d\bar{u}/dy)$, the Reynolds shear stress and the sum of these stresses, respectively. The results obtained by Kuroda and Kasagi are also indicated by the broken lines in these figures. Our computational results are in agreement with those of the spectral method.

Fig. 6(a) and (b) show the profiles of the mean temperature and the root-mean-square values of temperature fluctuation. These mean and rms values are in the non-dimensional form by using the friction temperature, $\theta_\tau[= q_w/(\rho_c c_{p_c} u_\tau)]$. Our results for the channel flow heat transfer in the cases of $Pr = 2.0$ and 1.5 are compared with those obtained by Kim and Moin (1989), and Kawamura et al. (1998), respectively. Our results in these two cases are in good agreement with these reference data. Thus, the computational methods used for the continuous-phase flow is verified from these results.

8.2. Secondary flow around droplets

We discuss the interaction between main flow and droplets for a short period by using some snapshots in this and the next section.

Fig. 7(a)–(c) demonstrate the velocity fluctuation, the contour map of temperature, and the ratio of local heat flux in the case with the droplets to that in the case without the droplets at the same instant on the (x, y)-plane including the centers of the droplets on the right-hand-side, respectively. The solid lines show the interface. In Fig. 7(b), the white area indicates a lower temperature region, while the black area indicates a higher temperature region. In Fig. 7(c), the local heat flux is higher than that in the case without the droplets in the black area.

Noticeable velocity vectors due to the gravitational force are seen inside and below the droplets in Fig. 7(a). The velocity of the upper droplet is slightly higher than

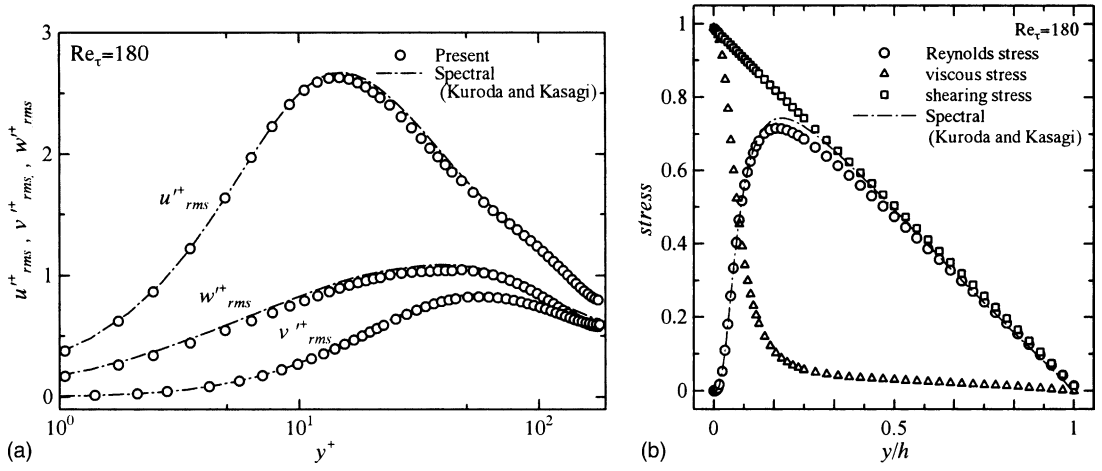

Fig. 5. Turbulence intensities and stresses: (a) streamwise, wall-normal and transverse intensities, (b) viscous shear stress, Reynolds shear stress and sum of these stresses.

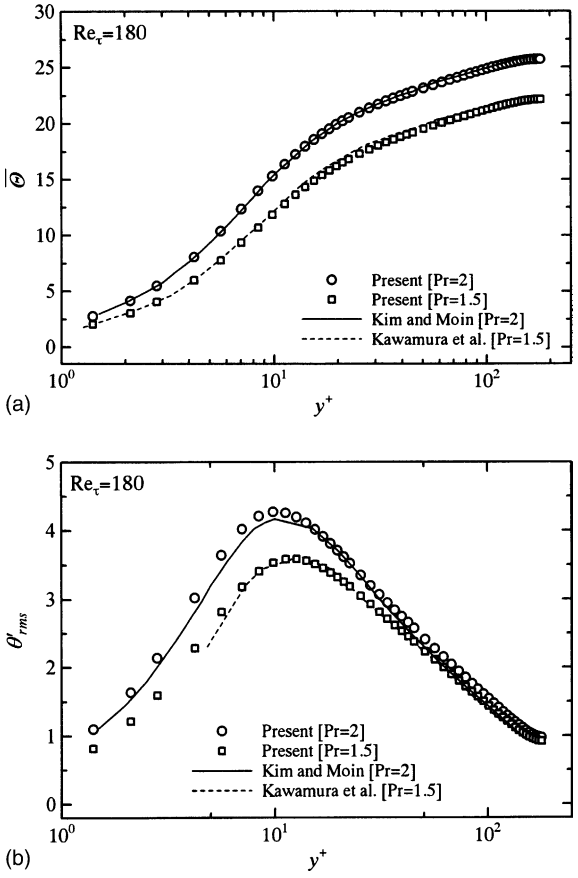

Fig. 6. Temperature profiles: (a) mean temperature, (b) root-mean-square of temperature fluctuation.

that of the lower droplet. This is because the upper droplet is inside the wake flow region of lower droplet where the impinging main flow is decelerated by the lower droplet. Similar reaction of the upper droplet to the lower droplet was observed in our recent measurement. The Reynolds numbers based on the relative velocities and the droplet diameters were in the range of 450–680. Their mean value is approximately equal to that measured for the hydrofluoroether droplets (Tajima, 2003).

The secondary flow is seen on both sides of the droplets. Noticeable upward secondary flow is seen between the lower droplet and the wall. The flow is accelerated in this region. The secondary flow in this region resembles a wall jet. Part of this jet-like flow changes direction to the outward and approaches the right bottom of the upper droplet. The downward velocity vectors of the upper droplet changes the direction by the jet-like flow. At the same time, the flow along the left-hand-side of the upper droplet becomes predominant. The upper droplet is found to move outward after this moment. Thus, the wake flow of the lower droplet affects directly the secondary flow and the motion of the upper droplet in the case of short distance between the droplets. This cannot be predicted by the previous simulation for a droplet. It should be noted that the similar motion of hydrofluoroether droplet with flow along the interface of facing away from the wall was observed in our previous measurement (Hagiwara et al., 2001).

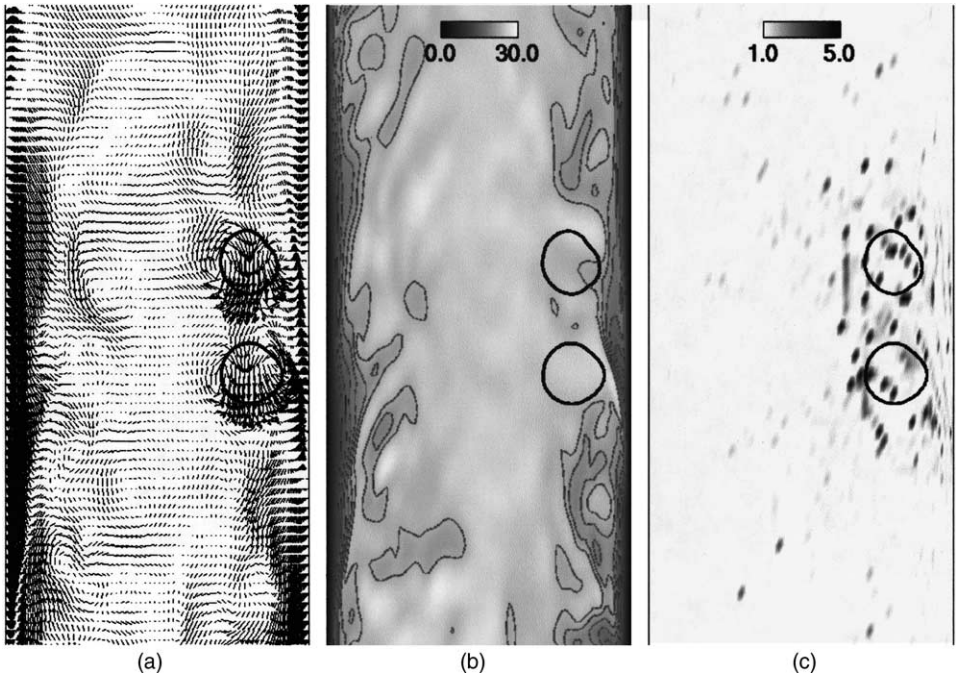

Fig. 7. Velocity fluctuation and contour map of temperature in a (x, y)-plane profile: (a) velocity fluctuation and interface (solid lines), (b) contour map of temperature (contour level = 13, 15, 17, 19, 21, 23) and interface (solid lines), (c) ratio of local heat flux in the case with droplets to that in the case without droplets.

The other part of the wall-jet-like flow passes through the gap between the wall and the upper droplet. Therefore, high-speed upward flow is seen in a wide region adjacent to the wall near the droplets.

Fig. 8(a) and (b) show the velocity vectors and the contour map of temperature on the central part of a cross-sectional (y,z)-plane below the cap of the lower droplets in the impinging flow region, respectively. Large-scale circulating motions are seen near the upper wall. These are the streamwise vortices identified by the method proposed by Jeong and Hussain (1995). Similar large-scale motion is seen in the lower-left region of the left-hand-side droplet where the developed streamwise vortex interacts with the droplet.

It is found that the impinging flow diverges 360° at the caps of the droplets. The highest value for the ratio of the Reynolds-shear stress product to the local Reynolds shear stress, $-u'v'/(-\overline{u'v'}(y))$, around the cap of the droplet was 1.2–8.1 times higher than that in the case without the droplets.

Fig. 9(a) and (b) indicate the velocity vectors and the contour map of temperature on a (y,z)-plane above the tail of the lower droplets in their wake regions, respectively. The droplet has already passed through the plane from above and is leaving from the plane. The broken lines show the projection of lower droplets. The flows from the wall to the wake region are observed. The flow for the left-hand-side droplet interacts strongly with the streamwise vortex, and part of the flow is involved in the vortex. It was confirmed by comparing Fig. 9(a) with the figure in the case without the droplets that the streamwise vortices were deformed by the droplets. In addition, small-scale streamwise vortices were attenuated by the droplets. Therefore, the near-wall droplets disturb the development of streamwise vortices.

Fig. 10(a) and (b) depict the velocity vectors and the contour map of temperature on a (y,z)-plane below the cap of the upper droplets in the impinging flow region, respectively. Fig. 10(a) is similar to Fig. 8(a) except for the upward flow above the right-hand-side droplet and

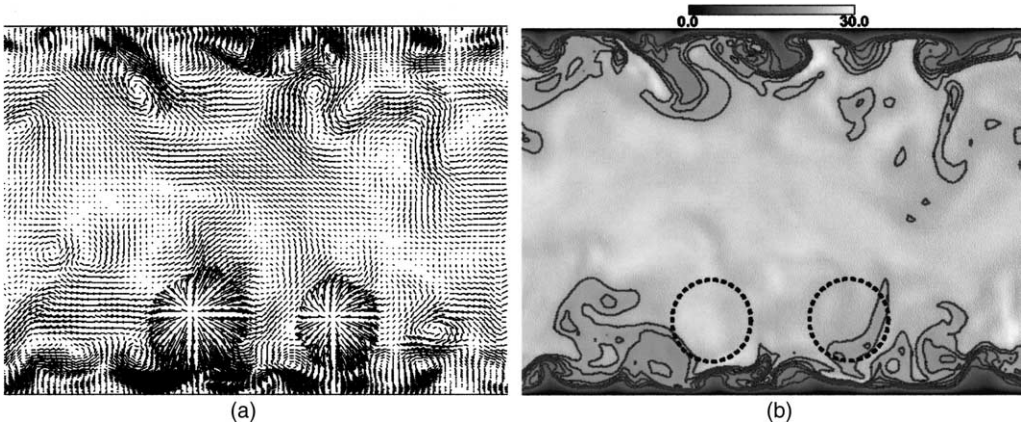

Fig. 8. Velocity fluctuation and contour map of temperature in the central part of a (y,z)-plane below the cap of lower droplets: (a) velocity fluctuation, (b) contour map of temperature (contour level = 13, 15, 17, 19, 21, 23) and projection of droplets (broken lines).

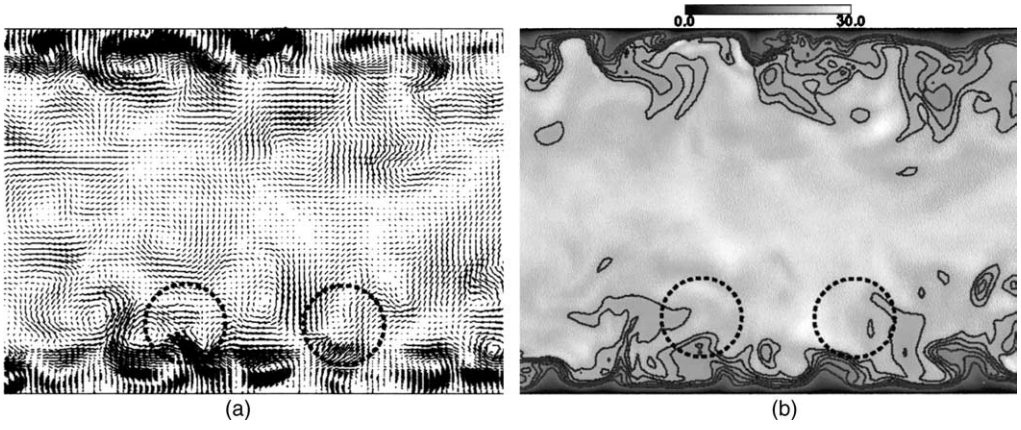

Fig. 9. Velocity fluctuation and contour map of temperature in the central part of a (y,z)-plane above the tail of lower droplets: (a) velocity fluctuation and projection of droplets (broken lines), (b) contour map of temperature (contour level = 13, 15, 17, 19, 21, 23) and projection of droplets (broken lines).

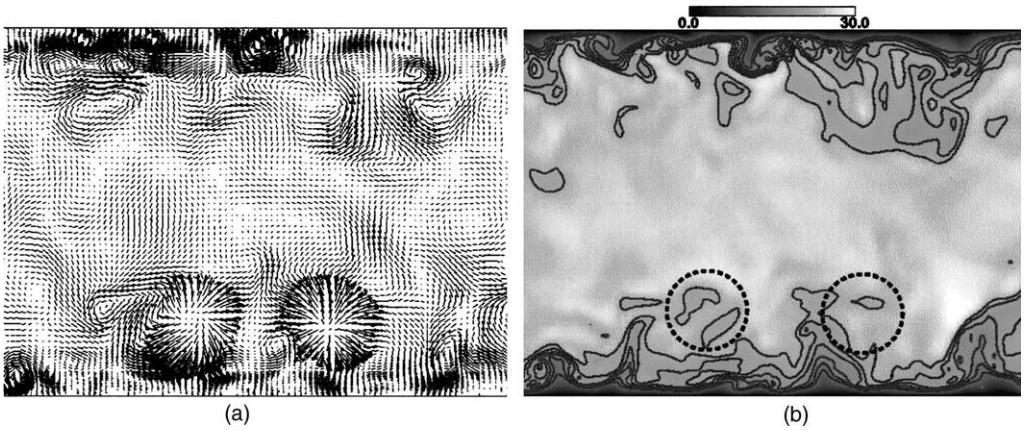

Fig. 10. Velocity fluctuation and contour map of temperature in the central part of a (y,z)-plane below the cap of upper droplets: (a) velocity fluctuation, (b) contour map of temperature (contour level = 13, 15, 17, 19, 21, 23) and projection of droplets (broken lines).

for flows along the interface and in the left direction for the left-hand-side droplet. The upward flow is associated with the secondary flow along the interface facing away from the wall shown in Fig. 7(a). The flow around the right-hand-side droplet is the result of modification of the streamwise vortex by the droplet.

Fig. 11(a) and (b) demonstrate the velocity vectors fluctuation and the contour map of temperature on a (y,z)-plane above the tail of the upper droplets in their wake regions, respectively. The droplet has already passed through the plane from above and is leaving from the plane. The broken lines show the projection of the upper droplets. A pair of counter-rotating fluid motion is observed between the right-hand-side droplet and the wall. This is due to the newly generated vortices from the interface. Similar vortices were predicted at the same location of interface for immiscible droplet (Iwasaki et al., 2001). In addition, a gathering flow is seen from the central region to the center of the wake flow region in the figure. This is caused by the secondary flow along the interface of facing away from the wall. A similar flow was observed and predicted in our previous study for an isolated descending droplet in upward flow (Hagiwara et al., 2001).

8.3. Modification of heat transfer mechanism by droplets

In Fig. 7(b), low temperature regions (light gray) spreads below the cap of the droplets. In Fig. 7(c), the local heat flux in some regions around the droplets is higher than that in the case without the droplets. Thus, the turbulent heat transfer mechanism is different from that without the influence of the droplet.

In Fig. 8(b), the high-temperature regions are very thin at the passage between the right-hand-side droplet and the wall. This was due to the Q4 event and the wallward component of the flow along the cap in Fig. 8(a) brought low-temperature fluid into the near-wall

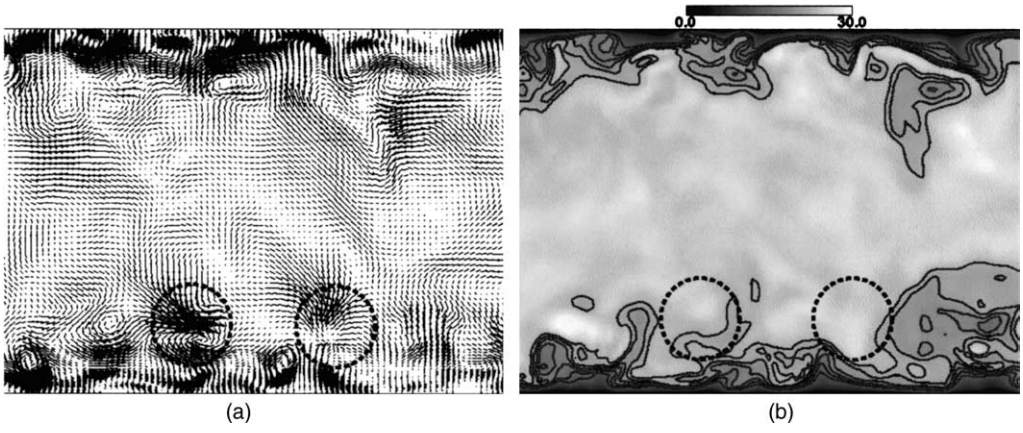

Fig. 11. Velocity fluctuation and contour map of temperature in the central part of a (y,z)-plane above the tail of upper droplets: (a) velocity fluctuation and projection of droplets (broken lines), (b) contour map of temperature (contour level = 13, 15, 17, 19, 21, 23) and projection of droplets (broken lines).

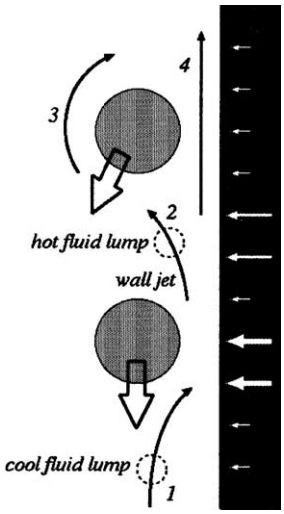

Fig. 12. Modification of heat transfer by secondary flows.

region. The highest value for the ratio of the product of the wall-normal velocity fluctuation and the temperature fluctuation to the local turbulent heat flux $v'\theta'/(\overline{v'\theta'}(y))$ around the cap of the droplet was 2.1–6.6 times higher than that in the case without droplets. Therefore, the secondary flow associated with the droplets is found to be effective for the enhancement of the near-wall heat transfer. This modification of heat transfer mechanism is drawn with the curved arrow (1) in Fig. 12.

The liftup of high-temperature fluid from the wall to the right-hand-side droplet is clearly seen in Figs. 9(b) and 11(b). The wall-jet-like flow in the outward direction transports fluid lumps with high temperature. This modification of heat transfer mechanism is drawn with the curved arrow (2) in Fig. 12. This liftup enhances heat transfer.

In Fig. 10(b), the high-temperature region adjacent to the wall becomes thinner compared with that seen in Fig. 8(b). This is due to the high-speed upward flow along the wall mentioned above. This modification of the heat transfer mechanism is drawn with the arrow (4) in Fig. 12. The low temperature regions induced by the impinging flow is not noticeable particularly for the left-hand-side droplet where two high temperature regions are seen inside the broken line. This was due to the Q2 event and the impingement of warm fluid was carried by the wall-jet-like flow mentioned above. This modification of heat transfer mechanism is drawn with the curved arrow (3) in Fig. 12. This also enhances the heat transfer.

The heat transfer enhancement by the secondary flows induced around the droplets is more noticeable than the heat transfer attenuation due to the modification or attenuation of streamwise vortices by the droplets.

9. Conclusions

The direct numerical simulation was carried out for a turbulent upward flow between two heating walls with four immiscible droplets. The interface was tracked by the modified VOF algorithm. The main conclusions obtained are as follows

1. The droplet induced several types of secondary flows. These flows increased the Reynolds shear stress product. These flows were attenuated by the adjacent droplet in the streamwise direction.
2. The small-scale streamwise vortices were attenuated near the droplets. The large-scale developed streamwise vortices were deformed by the droplets.
3. The product of wall-normal velocity fluctuation and the temperature fluctuation increased by the secondary flows. This shows an enhancement of turbulent heat transfer by the droplets.

Acknowledgements

This study was supported by the Japan Society for Promotion of Science through the Grant-in-Aid for Scientific Research (No. 14550181).

References

Hagiwara, Y., Takagaki, S., Yuge, T., 2003. Effects of a droplet on near-wall transport phenomena in turbulent downward liquid–liquid flow. J. Enhanced Heat Transfer 10 (1), 81–93.

Hagiwara, Y., Suzaki, T., Saegusa, D., 2001. Interaction between near-wall turbulence structure and immiscible droplets falling with wobbling motion in upward water flow. In: Proc. of 3rd Int. Symposium on Advanced Energy Conversion Systems and Related Technologies (RAN2001), (CD-ROM) pp. 409–416.

Hirt, C.W., Nichols, B.D., 1981. Volume of fluid method for the dynamics of free boundaries. J. Comput. Phys. 39, 201–225.

Inaba, H., Horibe, A., Ozaki, K., Yokoyama, N., 1998. Liquid–liquid direct contact heat exchange using a perfluorocarbon liquid for waste heat recovery (in Japanese). Trans. JSME 64B, 3838–3845.

Iwasaki, T., Nishimura, K., Tanaka, M., Hagiwara, Y., 2001. Direct numerical simulation of turbulent Couette flow with immiscible droplets. Int. J. Heat Fluid Flow 22, 332–342.

Jeong, J., Hussain, F., 1995. On the identification of a vortex. J. Fluid Mech. 285, 69–94.

Kadoguchi, K., 2002. Direct-contact boiling phenomena in a field with the continuous liquid–liquid interface. In: Progress in Transport Phenomena, pp. 285–289.

Kaviany, M., 1994. Principles of Convective Heat Transfer. Springer-Verlag, New York.

Kawamura, H., Ohsaka, K., Abe, H., Yamamoto, K., 1998. DNS of turbulent heat transfer in channel flow with low to medium–high Prandtl number fluid. Int. J. Heat Fluid Flow 19, 482–491.

Kim, J., Moin, P., 1989. Transport of passive scalars in a turbulent channel flow. In: André, J.-C., Cousteix, J., Durst, F., Launder, B.E., Schmidt, F.W., Whitelaw, J.H. (Eds.), Turbulent Shear Flows, vol. 6. Springer-Verlag, Berlin, Heidelberg, pp. 85–96.

Kuroda, A., Kasagi, N., 1992. Available from <http://www.thtlab.t.u-tokyo.ac.jp/index/html>.

Lee, J.M., 1987. Drop size formations in agitating system. In: Cheremisinoff, N.P. (Ed.), Encyclopedia of Fluid Mechanics, vol. 6, pp. 141–165.

Tajima, M., 2003. MS thesis, Kyoto Institute of Tech., 2003.

Tanaka, M., Takashina, Y., Hagiwara, Y., Nishimura, K., 1997. Evaluation in interaction between an immiscible droplet and a liquid laminar Couette flow using local mesh refinement. In: ISAC'97 High Performance Computing on Multiphase Flows, pp. 31–34.